A morphological analysis of activity-dependent myelination and myelin injury in transitional oligodendrocytes

Toth, Eszter; Rassul, Sayed; Berry, Martin; Fulton, Daniel

DOI:
10.1038/s41598-021-88887-0

Document Version
Publisher's PDF, also known as Version of record

Citation for published version (Harvard):
Toth, E, Rassul, S, Berry, M & Fulton, D 2021, 'A morphological analysis of activity-dependent myelination and myelin injury in transitional oligodendrocytes', *Scientific Reports*, vol. 11, no. 1, 9588.
https://doi.org/10.1038/s41598-021-88887-0

scientific reports

Check for updates

OPEN

A morphological analysis of activity-dependent myelination and myelin injury in transitional oligodendrocytes

Eszter Toth[1,2], Sayed Muhammed Rassul[1,3], Martin Berry[1] & Daniel Fulton[1]✉

Neuronal activity is established as a driver of oligodendrocyte (OL) differentiation and myelination. The concept of activity-dependent myelin plasticity, and its role in cognition and disease, is gaining support. Methods capable of resolving changes in the morphology of individual myelinating OL would advance our understanding of myelin plasticity and injury, thus we adapted a labelling approach involving Semliki Forest Virus (SFV) vectors to resolve and quantify the 3-D structure of OL processes and internodes in cerebellar slice cultures. We first demonstrate the utility of the approach by studying changes in OL morphology after complement-mediated injury. SFV vectors injected into cerebellar white matter labelled transitional OL ($_T$OL), whose characteristic mixture of myelinating and non-myelinating processes exhibited significant degeneration after complement injury. The method was also capable of resolving finer changes in morphology related to neuronal activity. Prolonged suppression of neuronal activity, which reduced myelination, selectively decreased the length of putative internodes, and the proportion of process branches that supported them, while leaving other features of process morphology unaltered. Overall this work provides novel information on the morphology of $_T$OL, and their response to conditions that alter circuit function or induce demyelination.

The speed of information transfer in axons is enhanced by myelination, with processing speed rising as axonal ensheathment increases[1,2]. These gains in signal transmission arise as a result of alterations in the electrical properties of myelinated nerve fibres, including reduced transmembrane capacitance and increased resistance. Collectively these changes increase the axonal length constant allowing depolarising current to spread over greater distances before requiring a boost from active depolarising currents. Consequently, conduction velocities in myelinated axons are enhanced significantly over those of unmyelinated axons of a similar caliber once a specific diameter, estimated at 0.2 µm, is exceeded[3].

Myelin formation and neuronal activity are intimately linked. Pharmacological blockade of neuronal activity reduces myelination in numerous in vitro and in vivo systems[4–6], while increased neuronal activity, induced either optogenetically[7], or via sensory input[8], has the opposite effect. This connection between circuit function and myelination, and the eventual contribution myelination makes to functioning of the recipient axon, has led to the concept of myelin plasticity, and an appreciation of the contribution it may make to cognitive function and dysfunction[9–12]. To study myelin plasticity, and evaluate the cellular and molecular mechanisms driving its expression, it is necessary to develop methods that enable a dynamic analysis of internode formation and characteristics under differing levels of axonal activity. Internode thickness and length are particularly relevant to these analyses[13]. Increases in myelin thickness simultaneously reduce the transmembrane capacitance charge, and the leak of cations from the axoplasm towards the extracellular space, which together increase the spread of depolarizing current along the axon towards the next node. Consequently, the axonal length constant increases allowing depolarizing current to travel further before requiring time and energy consuming boosts from active nodal currents. Intermodal length is therefore free to increase so that enhancements in conduction velocity scale with increasing internode length until they reach a 'flat maximum' from which no additional increases can be

[1]Neuroscience and Ophthalmology Research Group, Institute of Inflammation and Ageing, College of Medical and Dental Sciences, University of Birmingham, Edgbaston, Birmingham B15 2TT, UK. [2]School of Psychology, College of Life and Environmental Sciences, University of Birmingham, Birmingham, UK. [3]Physical Sciences of Imaging in the Biomedical Sciences Training Programme, University of Birmingham, Birmingham, UK. ✉email: d.fulton@bham.ac.uk

achieved[14]. Internode thickness and length are therefore important factors in determining axonal conduction velocities.

Although internode thickness is a key parameter controlling conduction velocity, its measurement is unsuited to a dynamic analysis, for example by live-imaging, since it requires the histological analysis of transected axons. Internode length, on the other hand, can be examined in transgenic reporter mice in which fluorescent protein (FP) expression is targeted to oligodendrocyte lineage cells (OL), or in OL labelled by FP expressing viral vectors. In the former setting, longitudinal in vivo two-photon microscopy has been used to visualise the morphologic responses of adult OL internodes labelled by membrane targeted green FP (mGFP)[15]. Interestingly, environmental enrichments designed to provoke increased neuronal activity, induced an increase in newly formed OL without affecting internode dynamics[15]. Indeed, the internodes of mature OL maintained a remarkable stability even when monitored over 50 days. This stability in OL morphology is not universal however since sensory deprivation reduces OL process length and internode number in the cortex of newly weaned mice (21 days)[8]. OL therefore seem to exhibit a greater degree of morphological plasticity at earlier stages of CNS development. Indeed, data from neonatal cortical slice cultures reveal a reduction in internode length following blockade of GABA-A receptors[16]. It is important to note that the majority of studies in this area have focused on cortical gray matter OL[7,8,15], and that in vivo imaging of deeper lying white matter structures represents a significant challenge to current imaging methodologies[reviewd in17]. For these reasons, the question of how neuronal activity alters OL and internode morphology in white matter, and how these effects vary across developmental ages and anatomical regions, remains an open question.

In this paper, we report the morphological analysis of neonatal white matter OL within a system amenable to prolonged pharmacological manipulations capable of either modulating neuronal activity or inducing OL myelin injury. To achieve this we adapted an approach involving the gliotropic subtype of the Semliki Forest Virus (SFVA7(74) (SFV)[18], previously used for labelling OL in cultured hippocampal slices[19], to label OL in the white matter of neonatal cerebellar slice cultures. Injection of SFV vectors encoding membrane targeted FPs into cerebellar white matter provided an efficient and rapid labelling of myelinating OL, the brightness and extent of which allowed the resolution of complex OL process arbors. OL image stacks were traced and the resulting 3-D reconstructions analysed to provide quantitative data on OL process length and branching, the length and spatial location of putative internodes, and the proportions of myelinating and non-myelinating process branches. The results provide new information on the morphology and activity-dependent development of transitional OL ($_{T}$OL), an intermediate stage of maturation linking pre-myelinating OL, in which all process branches (PB) are non-myelinating ($_{NM}$PB)[20], and mature myelinating OL ($_{M}$OL), in which it is expected that all PB are myelinating ($_{M}$PB). In this work, $_{T}$OL are defined as cells possessing a mixture of $_{NM}$PB and $_{M}$PB[19,20], and the term myelinating OL is used generically to include both $_{T}$OL and $_{M}$OL.

We have confirmed that this methodology resolves changes in $_{T}$OL morphology in slice cultures subjected to a complement-mediated injury. 3-D reconstructions obtained after complement injury revealed clear evidence of damage, including the fragmentation and loss of $_{T}$OL processes and internodes, consistent with myelin damage observed after myelin basic protein (MBP) staining. To analyse changes in morphology associated with neuronal activity, slices were subjected to a chronic treatment with tetrodotoxin (TTX). Immunohistochemical analysis showed that TTX treatment reduced the localization of MBP to cerebellar folia axons confirming that neuronal activity influenced myelination in these slice cultures[5]. This reduction in myelination was accompanied by changes in $_{T}$OL morphology that included a reduction in the length of putative internodes, and an increase in the proportion of PB that were $_{NM}$PB, implying that basal neuronal activity directs the differentiation of $_{T}$OL processes towards the production and elongation of internodes. Overall, this work demonstrates the suitability of organotypic brain slice cultures for the study of OL morphological plasticity and injury, and provides a foundation for work to track the dynamic response of OL processes arbors and internodes to changing physiological conditions, or pathological insults, in deep lying white-matter regions that are currently beyond the range of in vivo imaging methods.

Results

SFV vectors label myelinating OL in the white matter of neonatal cerebellar slice cultures. In our previous work we applied SFV vectors encoding farnesylated FP (eGFP-f) directly to the surface of cerebellar slice cultures to label glia[5]. Owing to the limited diffusion of viral particles through the tissue slice[21] this method predominantly labelled glia residing close to the upper surfaces of the slice, including NG2^{+} OPC and astrocytes, but very few cells with a morphology typical of myelinating OL. In the present work, we attempted to label myelinating OL in deeper regions of the slice by microinjecting SFV vectors into the white matter tracks of the folia (Fig. 1Ai) where myelinated Purkinje cell axons reside (see Supplementary Materials and Methods online). In agreement with previous studies in hippocampal slice cultures[19,22] these injections labelled glia with multiple parallel-aligned processes typical of myelinating OL (Fig. 1Aii). Immunostaining with antibodies to MBP (Fig. 1B) and MOG (Fig. 1C) revealed positive localization of these myelin proteins to SFV labelled OL (Figs. 1B, 2C), while staining of axons with anti-NF200 revealed close alignments of axons and the processes of SFV labelled OL (Fig. 1D). In addition SFV vectors illuminated the myelinating morphology of OL expressing CNPase-GFP transgenes[23] (see Supplementary Fig. S1 online). Taken together these data confirm that SFV labelling identified myelinating OL in the cerebellar white matter.

Morphological and immunohistochemical features that distinguish labelled myelinating OL from astrocytes. The injection of SFV vectors into hippocampal slice cultures labels glia displaying a morphology typical of astrocytes[18,24] with highly-ramified GFAP^{+} processes that are immunonegative for the OL marker RIP [18]. In addition to the OL described in Fig. 1, we also observed astrocyte-like glia following injection

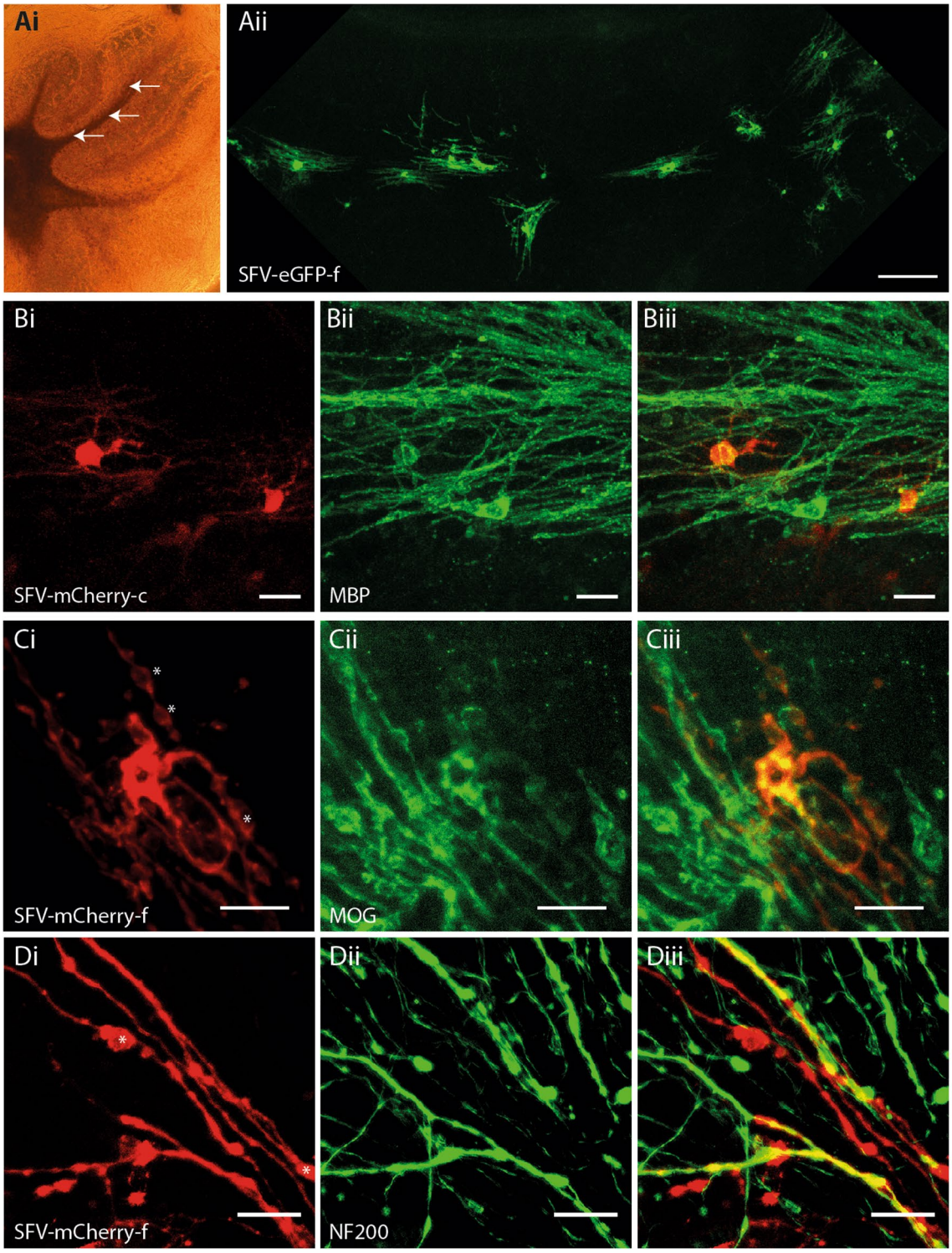

Figure 1. SFV transduces myelinating OL in cerebellar slice cultures. (**Ai**) Phase contrast image of a cerebellar slice culture illustrating white matter tracks and typical sites for SFV injections (arrows). (**Aii**) OL with a myelinating morphology are labelled throughout the entire white matter track of one folium 24 h after injection of SFV encoding eGFP-f. Magnification 10×, Scale bar 100 µm. (**B**) SFV labelled OL express MBP. (**Bi**) Cytoplasmic mCherry (mCherry-c) in two white matter cells with typical myelinating OL morphology. (**Bii**) MBP immunofluorescence in the field shown in (**Bi**). (**Biii**) Merged image indicating localization of anti-MBP (green) to the processes of the mCherry^{+} (red) cells depicted in (**Bi**). Magnification 20×, Scale bars in (**B**) panels 20 µm. C. SFV labelled cells localize MOG. (**Ci**) mCherry-f labelled white matter glial cell with myelinating morphology. (**Cii**) MOG immunofluorescence in the field shown in (**Ci**). (**Ciii**) Combined mCherry and MOG signals indicate colocalization of anti-MOG (green) and mCherry (red) signals. Magnification 40×, Scale bars in (**C**) panels 20 µm. (**D**) Axonal interactions of SFV labelled OL. (**Di**) High power (40×) image of processes (red) extending from an OL transduced with SFV-mCherry-f. (**Dii**) Axons (green) from the field depicted in Di labelled with anti-NF200. (**Diii**) Merge image indicating localisation of NF200 on SFV labelled processes (yellow). Asterisks in Ci and Di indicate mCherry-f labelled membrane bubbles. Scale bars in (**D**) panels 20 µm.

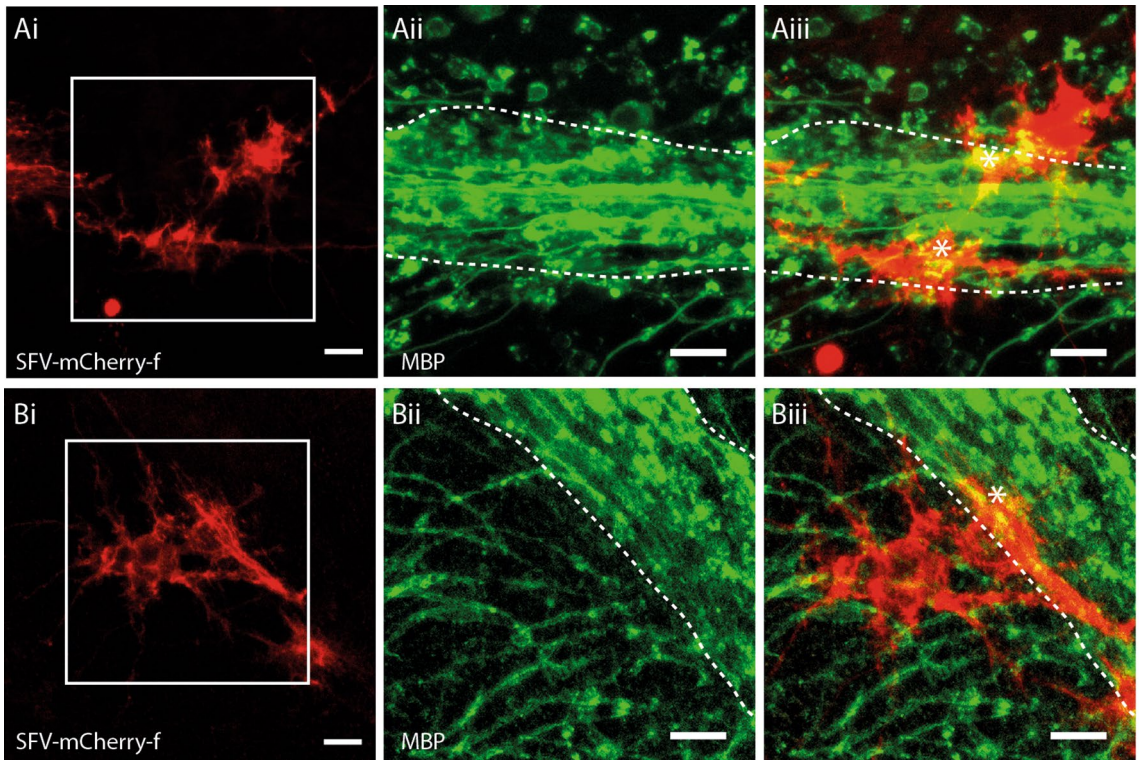

Figure 2. SFV transduced astrocytes are morphologically and antigenically distinct from OL. (**Ai**,**Bi**) mCherry-f labelled glia in cerebellar white matter exhibiting complex finely branching process fields typical of astroglia. (**Aii**,**Bii**) Enlarged view of the boxed areas shown in (**Ai**)/(**Bi**) showing the major white matter paths (dashed white lines) with MBP$^+$ OL processes (green) branching into the granule cell layer. (**Aiii**,**Biii**). Merged image showing mCherry-f fluorescence and MBP immunoreactivity from the same enlarged views shown in (**Aii**)/(**Bii**). White dashed lines indicate major white matter paths. In contrast to OL (Fig. 1) SFV labelled astrocytes lack cellular processes aligned in parallel with the major white matter tracks, or linear segments of MBP/process localization. Astrocytes exhibit patches of MBP co-localization (*) suggesting contact with MBP$^+$ profiles within cerebellar white matter. Scale bars in all panels 20 µm.

of SFV into cerebellar white matter (Fig. 2Ai,Bi). These cells were easily distinguished from OL by their distinct morphology, chiefly characterised by numerous finely branching processes that were not oriented in parallel with the major white matter paths in the folia (Fig. 2Ai, 2Bi). In addition, the processes of these cells lacked the linear segments of MBP localisation typical of OL (Fig. 2Aiii,Biii). In some cases small patches of MBP localization were present (Fig. 2Aiii,Biii), likely reflecting convergence between astrocytes and the processes of MBP$^+$ OL, as has been reported previously for NG2$^+$ glia[25]. Overall SFV-labelled astrocytes were easily distinguished from myelinating OL by their distinct appearance and the absence of linear stretches of MBP reactivity that characterized OL processes (Fig. 2Aiii,Biii).

Analysis of $_T$OL morphology and putative internodes. SFV labelled OL were traced to produce 3-D reconstructions (see Supplementary Movie S1 online and Supplementary Fig. S2 online). Using these 3-D reconstructions we quantified the number, length and branching of OL process arbors (see Supplementary Materials and Methods online) measured from 12 cells labelled by SFV-eGFP-f (see Supplementary Methods online for cell selection criteria). See Table (control study) for a summary of these morphological parameters. Myelinating OL arbor morphology varied from a few longitudinally arranged process arbors (Fig. 3A) to a complex collection of parallel-aligned longitudinally arranged processes (Fig. 3B). On average OL in cerebellar white matter had 7.67 (±0.78) process arbors (Fig. 3C) with an average length of 177 µm (±37.5) (Fig. 3D). These processes contained an average of 7.3 (± 1.05) branch points (Fig. 3E) leading to a maximum branch order of 7.25 (±0.60) (Fig. 3F). Using the criteria for identifying putative internodes (see Supplementary Methods online) all of the OL examined contained process arbors with a mix of $_{NM}$PB and $_M$PB (Fig. 3Aiii,Biii) placing these cells at the $_T$OL stage of maturation[20]. The membrane targeted GFP illuminated two interesting features on $_T$OL. First, fine PB were seen to arise from putative internodes (arrows in Fig. 3Ai/Aiii and Bi/Biii), an observation that agrees with previous reports showing fine extensions stemming from internodes in developing CNS tissues[19,26]. Internodal PBs are not typically observed on mature $_M$OL[27] and we discuss their possible remodeling from the transitional to the adult form in the Discussion. Second, $_T$OL process arbors exhibited numerous bubble-like membrane protrusions (asterisks on Fig. 1Ci,Di, Fig. S2a, Fig. S3a) reminiscent of membrane bubbles described previously on developing OL[26]. Quantification of $_{NM}$PB and $_M$PB revealed that the majority of process branches were non-myelinating (ratio $_{NM}$PB/TB 0.76; ratio $_M$PB/TB 0.24). SFV labelled $_T$OL had an average of 5.08 (±0.45) internodes/

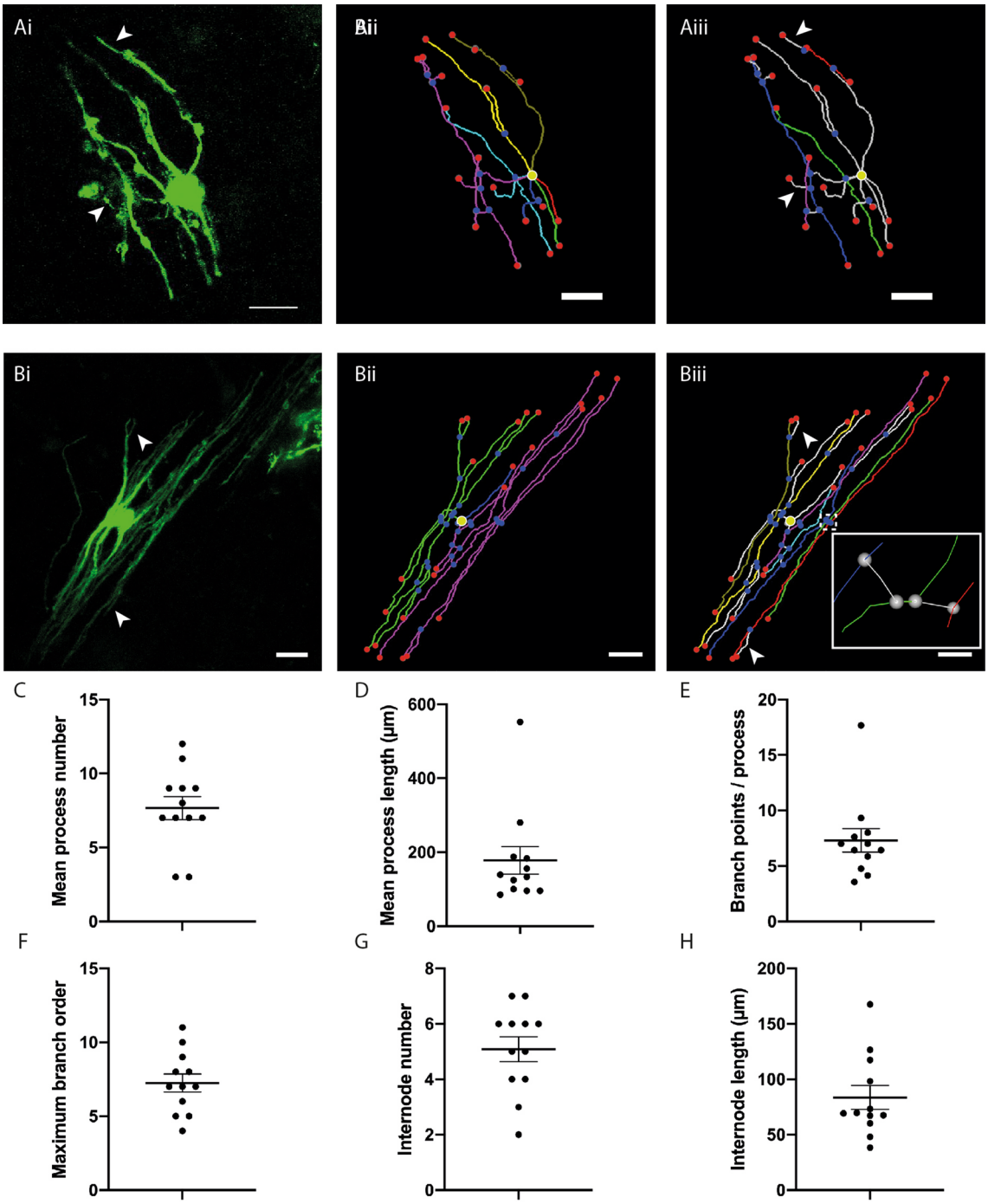

Figure 3. 3-D reconstructions of SFV-labelled OL and quantification of OL process morphology. (**Ai**) Maximum projection showing eGFP-f expression in a relatively simple white matter OL transduced with SFVA7(74). (**Aii**) 3-D reconstruction of the cell shown in (**Ai**). Segment colours (cyan, blue, green, yellow, gold, red, purple) indicate seven individual process arbors. Yellow circle indicates position of cell body. (**Aiii**) Reconstruction of the cell shown in (**Ai**) indicating position of four identified internodes (blue, purple, green, red). (**Bi**) Maximum projection showing eGFP-f expression in a relatively complex OL. (**Bii**) 3-D reconstruction for the cell shown in (**Bi**). Segment colours (blue, green, purple) indicate three individual process arbors. (**Biii**) Reconstruction of the cell shown in Bi indicating seven putative internodes (cyan, blue, green, yellow, gold, purple, red). Individual processes (green and purple in **Bii**) support multiple putative internodes. Inset: Expanded view of area indicated by dashed box reveals the initiation of internodes from neighboring internodes via fine connecting processes (white segments). Scale bars in (**A**) and (**B**) 20 µm. (**C**–**H**) Scatter plots displaying features of OL process morphology: mean process number per OL (7.67 ± 0.78) (**C**), mean process length (178 ± 37.5 µm) (**D**), average branch points per process (7.3 ± 1.05) (**E**), maximum branch order per process (7.25 ± 0.60) (**F**), mean internode number per cell 5.08 ± 0.45 (**G**), and mean internode length (83.7 ± 10.71 µm) (**H**). Arrows in (**Ai**)/(**Aiii**) and (**Bi**)/(**Biii**) indicate fine branches stemming from putative internodes. In (**Aii**–**iii**) and (**Bii**–**iii**) red and blue spheres indicate segment end-points and junction points respectively. Yellow circles indicate position of cell body. Data expressed as means ± SEM.

	(1) Control study	(2) TTX study		
		Control	TTX	*P*
Process arbors				
Number	7.7 (±0.45)	7.4 (±0.52)	7.9 (±0.61)	0.57[T]
Length (μm)	178 (±37.50)	179 (±16.50)	181 (±11.45)	0.94[T]
Total branches (TB)	25.3 (±3.11)	20.5 (±1.15)	24.6 (±1.86)	0.06[T]
Maximum branch order	7.3 (±0.61)	7.0 (±0.5.97)	7.8 (±0.58)	0.30[T]
Internodes				
Number	5.5 (4–6)	6 (4–7)	5 (3.5–6)	0.29[U]
Length	69.5 μm (±10.71)	85 μm (68–101)	54 μm (39–81)	0.0002[U]
Minimum order	1.2 (±0.11)	1 (1–1)	1 (1–1)	0.45[U]
Maximum order	5.1 (±0.57)	5 (±0.49)	4.5 (±0.46)	0.54[T]
Mean order	2.7 (±0.21)	2.9 (±0.21)	2.9 (±0.21)	0.76[T]
$\bar{x}$ internodes/process	2.2 (±0.34)	3 (2–4)	2 (2–3)	0.27[U]

Table 1. Morphology of $_{T}$OL. Minimum and maximum order refers to order of initiating branch. (1) relates to data shown in Fig. 3, (2) relates to data shown in Fig. 6. Values are Mean ± SEM. *P* values report comparison of Control and TTX data. [T] indicates unpaired *t* test, [U] indicates Mann–Whitney *U* test.

cell (Fig. 3G), with a mean internode length of 83.7 μm (range 38.7–167.6 μm) (Fig. 3H). $_{T}$OL internodes were contained within an area extending an average of 36.5 μm (range 23.9–42.7 μm) perpendicular to the white matter path, and 17.33 μm (range 15.6–22 μm) in the Z axis forming a flattened tube-like space. The spatial arrangement of internodes was examined by analyzing the branch ordering of internode initiation sites, and quantifying the maximum number of internodes per $_{T}$OL process arbor (Table 1, control study). Internodes initiated from branches located across a wide range of orders (range 1st to 9th order), while the number of internodes associated with each $_{T}$OL process varied from a single internode (Fig. 3Aii,Aiii), to process arbors supporting up to 5 internodes interconnected by fine connecting branches (Fig. 3Biii, inset) (see "Discussion").

Morphological analysis of OL after complement-mediated myelin injury. We examined the ability of the tracing method to detect changes in OL morphology in cerebellar slices exposed to a complement-mediated myelin injury[28] (see Supplementary Materials and Methods online). Consistent with an injury to OL and myelin, MBP staining of complement treated slices revealed discontinuous segments of myelin with a fuzzy appearance, while control slices treated with complement alone, or an IgG isotype control, displayed continuous MBP^{+} segments with sharply defined profiles (see Supplementary Fig. S3 online). To determine how complement injury affected the morphology of OL, SFV vectors encoding an mCherryMBP fusion protein were injected into cerebellar white matter 24 h after the onset of the injury treatment. OL tropism for the mCherryMBP transgene was confirmed in slice cultures prepared from CNPase-GFP OL reporter mice[23], where it was targeted to $_{T}$OL expressing the CNPase-GFP^{+} transgene (Fig. 4Ai–iii). Although the mCherryMBP label provided a strong signal that clearly illuminated the process arbors of transduced OL, the fluorescence exhibited a distribution that was distinct to the other SFV-delivered proteins, e.g. eGFPf (Fig. 1Bi,Ci), in being enriched at specific regions within the process arbors of $_{T}$OL (Fig. 4Ai). Despite this punctate labelling, the mCherryMBP signal was suitable for tracing, with reconstructions from the non-injured control condition revealing numerous parallel aligned process arbors and putative internodes as expected of myelinating $_{T}$OL (Fig. 4Aiv; see supplementary movie S2 online). In contrast, analysis of $_{T}$OL in the complement injured slices showed clear signs of cellular damage characterized by the fragmentation of process arbors (Fig. 4Bi). This injury was evident in 3-D reconstructions, where intact process arbors were scarce, disconnected SFV labelled segments were frequent, and internodes were not detected (Fig. 4Biv; see supplementary movie S3 online).

Inhibition of neuronal activity reduces myelination in cerebellar white matter. To determine whether the SFV tracing method was sensitive to changes in myelination the morphology of OL was assessed after pharmacological blockade of neuronal activity. We have previously reported that sustained incubation in TTX for 48 h reduced myelination in cerebellar slice cultures[5]. Considering the variability in internode number and length obtained from SFV labelled OL (Fig. 3G,H), we examined the effect of a longer reduction in neuronal activity after incubation in TTX for 7 days. We first confirmed the effects of this treatment on axonal density and myelination by immunofluorescent staining for NF200 and MBP, respectively (Fig. 5A,B) (see Supplementary Materials and Methods online). The averaged NF200 pixel area for slices treated with TTX was slightly reduced compared to controls (Fig. 5C) ($P < 0.05$) suggesting a reduction in the density of axons in TTX treated slices. MBP/NF200 co-localisation was also reduced in TTX-treated slices indicating a reduction of myelination in folia white matter (Fig. 4D) ($P < 0.001$). Importantly, the reduction in myelination was independent of the effects on axonal density since co-localisation was normalised against axonal density (see Supplementary Materials and Methods online).

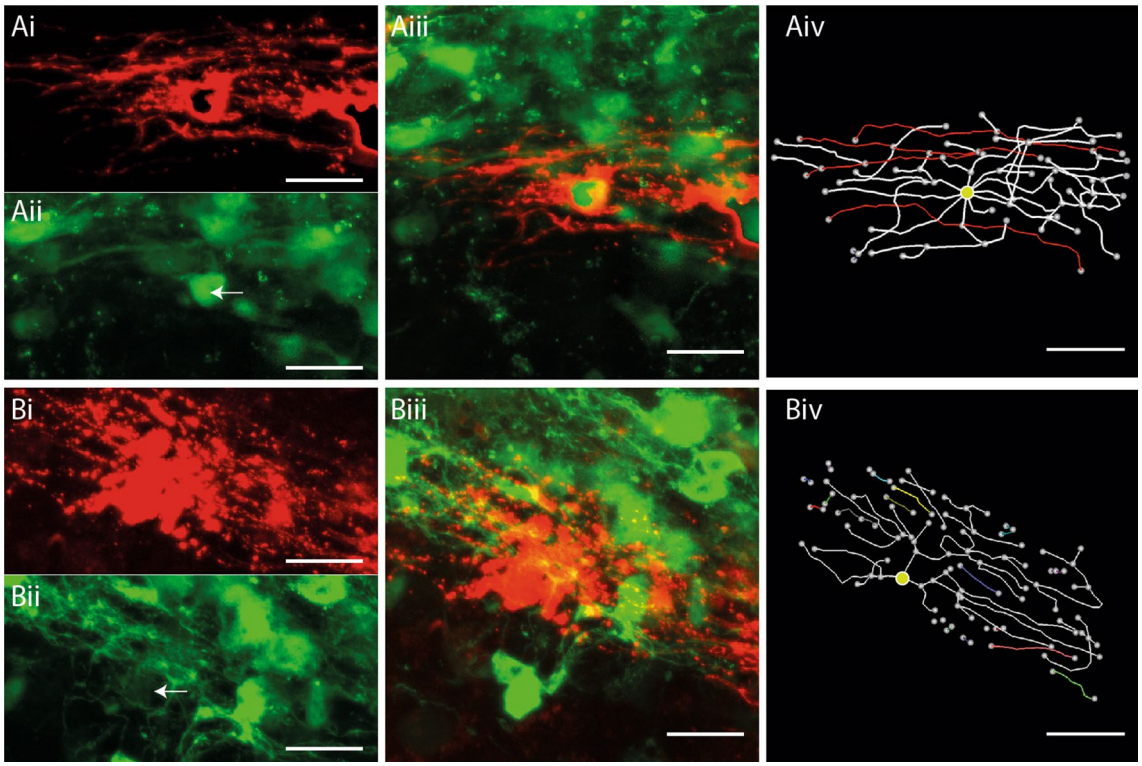

Figure 4. Complement mediated injury destroys internodes on SFV labelled OL. (**A**) Reconstruction of an SFV labelled OL expressing the CNPase-GFP transgene in a complement control treated slice. (**Ai**) mCherryMBP fluorescence reveals an OL with a typical myelinating morphology. (**Aii**) CNPase-GFP signals imaged from the field shown in (**Ai**) (white arrow indicates position of the mCherry^{+} OL). (**Aiii**) Merged image of the field shown in (**Ai-ii**) confirms co-localisation of mCherry (red) and CNPase-GFP (green) signals. (**Aiv**) 3-D reconstruction and analysis reveals 4 internodes (red) on the OL shown in (**Ai–iii**). (**B**) Morphological analysis of an A774 labelled OL following complement injury. (**Bi**) mCherry-f labelled OL with degenerating processes. (**Bii**) CNPase-GFP signals imaged from the field shown in (**Bi**). White arrow indicates position of mCherry^{+} OL shown in (**Bi**). (**Biii**) Merged image reveals localization of mCherry (red) and CNPase-GFP (green) signals. (**Biv**) Reconstruction and analysis of the cell shown in (**Bi–iii**) reveals fragmented processes (coloured segments) and the absence of internodes. Yellow circles indicate position of cell body. Scale bars in (**A**) and (**B**) 20 μm.

Neuronal activity influences $_{T}$OL process arbor morphology. Having confirmed that a 7-day incubation with TTX reduced myelination in cerebellar slice cultures, we examined whether sustained inhibition of neuronal activity altered the morphology of SFV labelled $_{T}$OL. Representative reconstructions of $_{T}$OL from control and TTX treated slices are displayed in Fig. 6A,B, and 3-D, movies of these cells can be viewed online (see supplementary movie S4 and S5 online), respectively. TTX treatment had no effect on the mean number, length, or maximum branch ordering of $_{T}$OL process arbors (Table 1, TTX study). In contrast, the average number of TB tended to be higher in TTX treated $_{T}$OL, although this trend did not reach statistical significance ($P=0.06$) (Fig. 6C). In agreement with the data on myelination (Fig. 5D), TTX treatment decreased the length of putative internodes ($P<0.001$) (Fig. 6D) but not their number ($P=0.29$) (Table 1, TTX study). To explore the morphology of $_{T}$OL further we analysed the ratios $_{NM}$PB/TB and $_{M}$PB/TB on control and TTX treated $_{T}$OL. TTX treatment produced complementary changes on these parameters, increasing the ratio $_{NM}$PB/TB (Fig. 6E) ($P<0.01$), while decreasing the ratio $_{M}$PB/TB (Fig. 6F) ($P<0.001$). These results, taken together with the lack of change in mean internode numbers (Table 1, TTX study), imply that the additional TB observed following TTX (Fig. 6C) fail to generate myelinating segments (Fig. 6C). We also examined whether neuronal activity influenced the spatial arrangement of internodes by quantifying the rank order of internode initiation sites. TTX had no effect on the spatial arrangement of internode initiation sites, with neither the minimum, maximum or average rank of initiation being altered between control and TTX treated $_{T}$OL (Table 1, TTX study). Similarly, TTX treatment had no effect on the maximum number of internodes per process arbor (Table 1, TTX study).

Discussion

We have used SFV labelling to develop new findings on the activity-dependent maturation of $_{T}$OL, and their response to complement-mediated injury. We show that SFV labelling in neonatal cerebellar slice cultures provides a platform for analyzing the effects of demyelinating injuries and altered axonal activity on $_{T}$OL process morphology, and internode number and length. This approach has several useful features. First, the use of

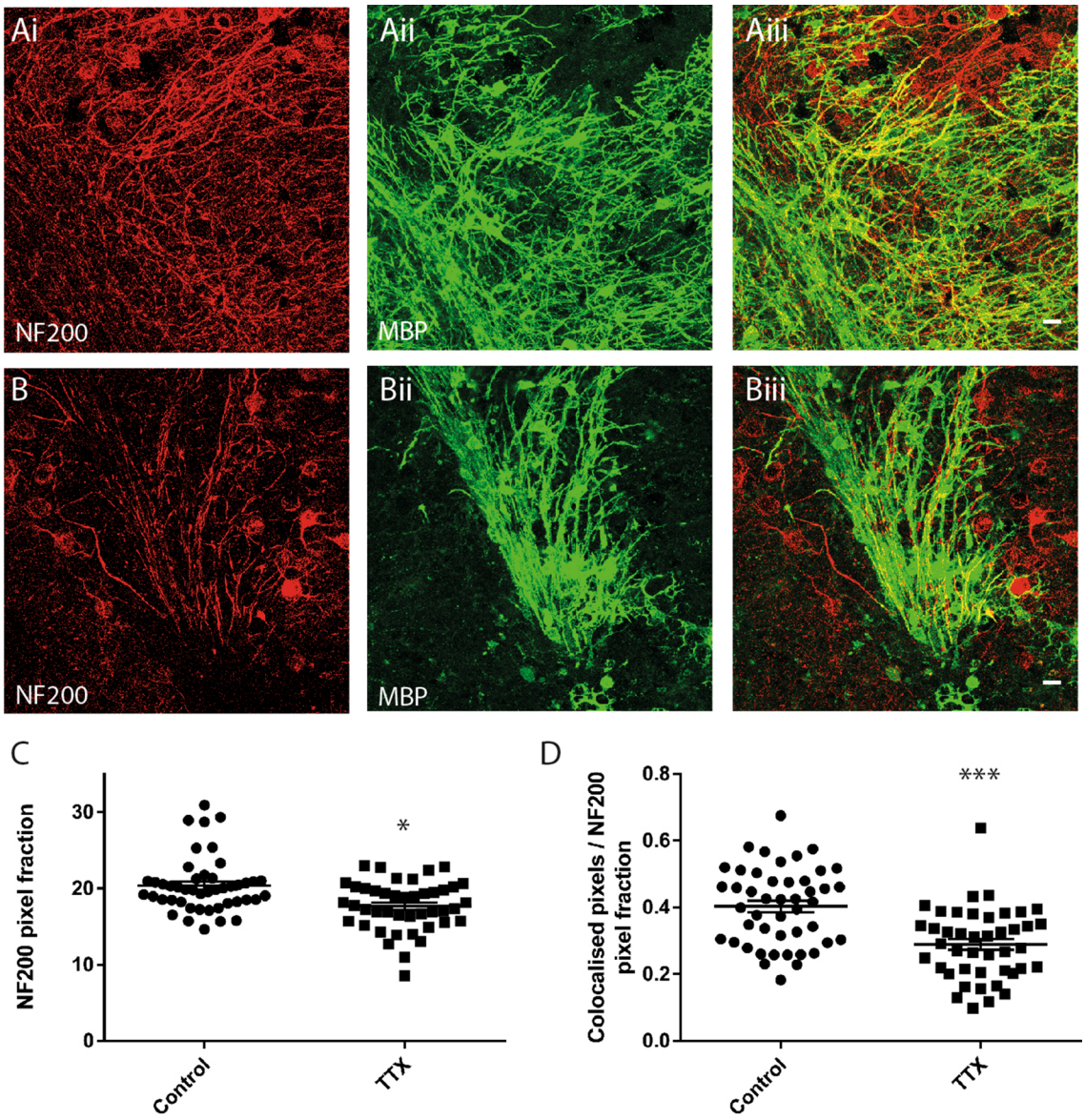

Figure 5. Sustained inhibition of neuronal activity reduces myelination of cerebellar white matter. (**A**,**B**) Maximum projection images from representative control (**A**) and TTX (**B**) treated cerebellar slices showing immunofluorescent signals for anti-NF200 (**Ai**,**Bi**) anti-MBP (**Aii**,**Bii**), and co-localisations used to quantify myelination (**Aiii**,**Biii**). (**C**) Quantification of anti-NF200 signals. Mean NF200 pixel fraction is reduced by TTX (Control 20.4 ± 0.5, TTX 17.7 ± 0.5). (**D**) Average MBP/NF200 ratios normalized against the NF200 signal are significantly reduced by TTX (Control 0.4 ± 0.02, TTX 0.29 ± 0.02). Scale bars in (**A**) and (**B**) 20 µm. * and *** Significance $P < 0.05$ and $P < 0.001$, respectively. Data expressed as means ± SEM.

organotypic slice cultures allows pharmacological modulation of neuronal function, and OL viability, within a system in which the in vivo arrangement of neuronal and glial cells is well preserved. Second, the slice cultures provide an opportunity to image OL in deep lying white matter structures, such as those of the cerebellum, that are beyond the reach of current in vivo imaging methods (reviewed in[17]). Third, SFV labelled slices are amenable to live-imaging[19], thus they may be exploited in imaging-based screening studies focused on dissecting the mechanisms regulating the effects of local circuit activity and CNS injury on OL and internode morphology.

SFV labelling in the white matter of cerebellar slice cultures revealed cells whose morphology and antigenic profile identified them as differentiated OL. The use of membrane tethered FPs enabled tracing and analysis of OL morphology revealing cells with complex process arbors incorporating multiple branch points, and giving rise to both $_{NM}$PB and $_{M}$PB, the latter of which were identified as thickened longitudinal segments of membrane arising from fine connecting branches. This combination of complex process fields with both $_{NM}$PB and $_{M}$PB identifies these cells as $_{T}$OL positioned between pre-myelinating and $_{M}$OL[19,20]. In support of this classification, SFV labelled OL share morphological characteristics with 'immature OL' labelled in rat optic nerves[27,29]. Moreover, the present work, and that of previous studies describing $_{T}$OL/immature OL phenotypes[20,27,29], did so in tissues of a similar

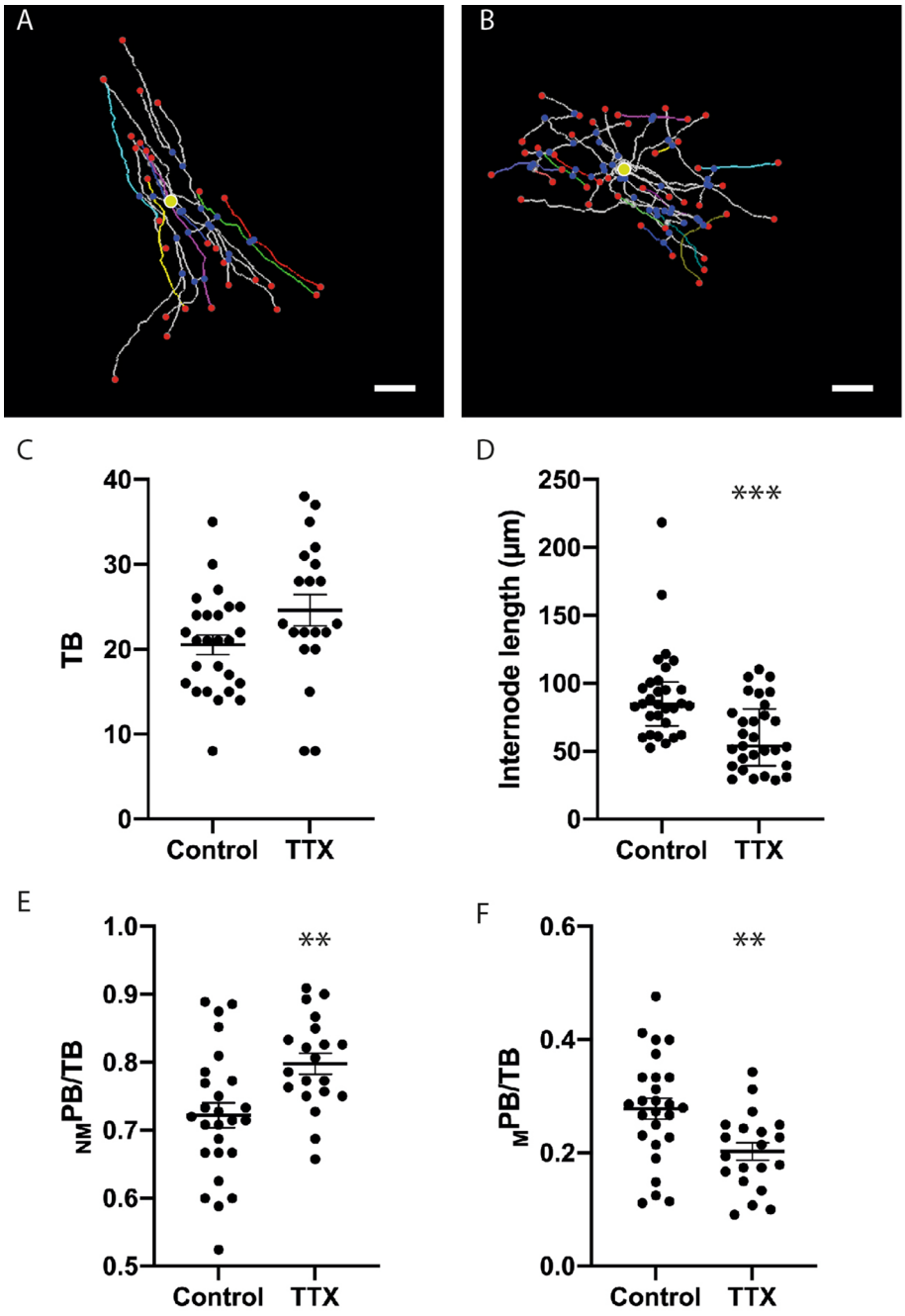

Figure 6. Sustained inhibition of neuronal activity alters OL morphology. (**A**,**B**) Representative 3-D reconstructions of OL from control (**A**) and TTX (**B**) treated cerebellar slices showing internodes selected for quantification (**A** cyan, blue, green, red; **B** blue, green, red) and cell bodies (yellow circles). (**C**) Tendency towards an increased numbers of branches per cell for TTX treated $_{T}$OL (Control 20.5 ± 1.15, TTX 24.6 ± 1.86). (**D**) TTX treatment reduced the median internode length of $_{T}$OL (Control 84.7 µm (68.6–101), TTX 53.8 µm (39.3–81.2). (**E**,**F**) TTX treatment induced complementary changes in the ratio $_{NM}$PB/TB (**E**) (Control 0.72 ± 0.02, TTX 0.80 ± 0.02) and $_{M}$PB/TB (**F**) (Control 0.28 ± 0.02, TTX 0.20 ± 0.02). Scale bars in (**A**) and (**B**) 20 µm. ** Significance $P < 0.01$, *** Significance $P < 0.001$. In (**A**) and (**B**) red and blue spheres indicate segment end-point and junction points respectively. Yellow circles indicate position of cell body. Data in (**C**), (**E**) and (**F**) expressed as means ± SEM, data in (**D**) expressed as median ± interquartile range.

age (e.g. postnatal CNS tissues P5–14), thus the OL labelled by SFV injections in cerebellar white matter are of an intermediate maturity between pre-myelinating and $_{M}$OL.

SFV labelling of $_{T}$OL with membrane-targeted FPs revealed morphological features recognized in other developing CNS systems. First, SFV labelled processes exhibited numerous membrane protrusions that mirror the membrane bubbles observed to travel along the processes of immature OL as they begin to ensheath axons[26]. Interestingly, immunostaining with anti-MBP revealed similar bubble-like features in our slice cultures (Fig. S4A,B) providing support for their involvement in the process of membrane deposition during the early stages of myelination[26]. Second, SFV labelling revealed fine PBs arising from putative internodes. Similar branches are apparent on the developing internodes of a number of immature myelinating systems including hippocampal slice cultures ([19] their Fig. 7A), embryonic spinal cord cultures ([26], their Fig. 2A), and larval zebrafish spinal cord ([30], their Fig. 2B). In contrast, internodal PB appear to be absent from myelin sheaths in adult CNS tissues[15,29] suggesting their resorption during CNS maturation. The present data, and that from a previous study of neonatal medulla[20], suggest that during development these internodal PB may myelinate since process arbors appeared to support multiple internodes interconnected by fine process extensions. However, despite the fine labelling provided by the SFV vectors, we cannot rule out the possibility of unresolved PB connections to the cell body. Certainly, internodal connections are difficult to reconcile with the current models of myelination (reviewed in[17]), and are not expected in mature OL where individual internodes are generally considered to arise from independent PBs[27]. Given the immature nature of the tissues under evaluation, interconnected internodes may exist as a transient feature prior to full OL maturation with additional sheaths being resorbed over time so that the final $_{M}$OL attains a morphology lacking interconnected internodes. In agreement with this view Butt and Ransom observe that the numerous parallel processes present on immature OL are lost in the mature form[27]. We attempted to examine this possibility in our system by injecting SFV vectors into older cerebellar slice cultures (~ 21 DIV). Repeated attempts failed to label OL in these cultures while similar injections continued to label OL in younger slices (~ 7 DIV) (data not shown). Taken together, these observations suggest that the glial tropism of SFV declines in maturing cerebellar slices rendering its use in investigating this question unfeasible.

Although several studies have described the morphology of $_{T}$OL[19,20], the present work is the first to analyse the spatial distribution of internode initiations with respect to branch ordering. Initiation points were not restricted to the primary branch, but occurred in a wide range of orders. These findings imply that the potential for internode initiation is present at all orders, and that transport mechanisms for myelin basic protein mRNA, which undergoes local translation at sites of myelination[31] (reviewed in[17]), are capable of delivering MBP mRNA to all orders of a process arbor.

SFV labelled $_{T}$OL possessed an average of 5 internodes (range 1–12), lower than comparable data obtained in vivo, which consistently report around 20 internodes per OL[27,29,32,33]. These in vivo studies have largely been pursued in the adult optic nerve where $_{M}$OL are expected to predominate, thus the lower number of internodes reported here may reflect the immature nature of the $_{T}$OL under study. Interestingly, measurements from a number of different adult CNS tissues revealed that OL in the cerebellum possess the fewest internodes[34], although this number is still fourfold greater than that reported in the present work. Whether $_{M}$OL in our slice cultures eventually achieve a comparable number of internodes remains to be seen, although the SFV tropism changes described above for older slice injections suggests that a different approach would be required to investigate this question.

The typical length of putative internodes measured from $_{T}$OL in cerebellar slices (~ 80 to 90 µm) are marginally shorter than those measured from cerebellar OL in vivo[34] where a distribution centered around ~ 100 µm is observed. Chong et al.[34] also used sparse OL labelling with a membrane targeted GFP to accurately resolve the 3-D morphology of OL and their internodes. The similarity in these approaches, and the resulting data, provide confidence in the methods we have used to identify and quantify internodes in $_{T}$OL. Our ex vivo measurements of cerebellar internode lengths are considerably longer than those obtained from neocortical slice cultures (mean 49 µm[16]). Interestingly, cortical internodes measured in vivo fall in a similar range to that measured ex *vivo* (~ 50 to 60 µm[34]) indicating that regional variations in internode length observed in vivo are preserved in slice cultures.

Our results provided new insights into complement-mediated injury in OL. 3-D analysis of SFV labelled $_{T}$OL enabled us to resolve the degeneration and loss of process arbors in slice cultures subjected to complement-mediated demyelinating injury. A significant outcome for this work was the absence of identifiable internodes after complement-induced injury, an observation that corresponded with a degradation in the integrity of myelin segments visualized by MBP staining. Previous studies imaging complement injury in slice cultures have used slices from OL reporter mice where transgene expression is present in all OL[28,35]. Thus parameters, such as process arbor morphology and internode number or length, could not be resolved at the single cell level. This work is therefore the first to provide a description of complement-induced OL injury at the level of single OL. These advances are important since auto-antibodies directed against myelin antigens, for example MOG (the myelin epitope targeted in the present work), are associated with OL injury and demyelination in multiple sclerosis[36,37]. Moreover, cerebellar slice cultures have recently been used to investigate the pathogenicity of recombinant auto-antibodies derived from the CSF of MS patients[35], and are gaining recognition as a useful tool for mechanistic studies into human demyelinating disease. In this context, live-imaging studies of SFV labelled OL could yield new information on the time-course OL injury, and be adapted to provide a platform for screening oligoprotective compounds.

The analysis of SFV labelled $_{T}$OL enabled the influence of neuronal activity to be studied during the early stages of myelination. Sustained treatment with TTX diminished the localization of MBP signals on cerebellar axons agreeing with our earlier work where a briefer incubation produced similar effects on myelination[5]. Analysis of SFV labelling after TTX treatment allowed us to correlate changes in the morphology of $_{T}$OL with reduced myelination. While not affecting the number of process arbors, blockade of neuronal activity appeared to promote a modest increase in process branching that was accompanied by a strong reduction in the proportion of process branches supporting internodes ($_{M}$B/TB), a ratio that is expected to increase as OL differentiate into a fully mature myelinating phenotype in which all processes support internodes[20]. These observations imply

that neuronal activity guides the morphological differentiation of OL such that growth is channeled towards the production of internodes on arbors receiving activity-dependent cues from target axons. When these cues are absent, growth may be invested in the generation of additional process arbors and non-myelinating branches at the expense of myelinating segments.

We detected similar numbers of putative internodes in control and TTX treated slices implying that reductions in myelination are not related to a reduction in the number of internodes per se. These observations differ to in vivo findings from a social isolation paradigm designed to reduce neuronal activity, where reductions in myelination in the medial prefrontal cortex were accompanied by a decrease in the number of internodes[8]. Differences in experimental approaches may explain these contrasting effects. TTX, as used here, will entirely block the activity of excitatory and inhibitory (GABAergic) neurons, while social isolation is likely to produce more nuanced effects that could differentially affect excitatory and inhibitory circuits. In this regard, recent work from neocortical slice cultures has revealed an involvement of endogenous GABAergic signaling in cortical myelination[16], with blockade of GABA-A receptors increasing the number of OL and boosting myelination. Interestingly, TTX prevented these changes, but had no effect on OL numbers when applied alone suggesting that GABA influences neocortical OL through a combination of activity-dependent and independent mechanisms. These findings contrast with data from the cerebellum where TTX promoted both OPC proliferation and differentiation[5]. Thus, clear differences seem to exist in the mechanisms regulating OL populations in the cerebellum and neocortex which may explain the differing morphological responses shown by OL in these regions.

TTX treatment reduced the length of internodes produced by cerebellar $_{T}$OL. This finding agrees with in vivo data from mouse optic nerve where monocular deprivation, or the genetic inhibition of vesicle release, lead to reductions in internodal length[38]. These findings from cerebellar slices, and optic nerve, suggest the involvement of an activity-dependent axonal signal during the elongation of myelin sheaths. However, as suggested by Hamilton et al.[16], reductions in internodal length may also reflect the outcome of increased competition among OL for a limited number of target axons. Indeed, blockade of neuronal activity in both systems produces an increase in the differentiation of OL[5], and in cerebellar slices this may be accompanied by a small reduction in axonal density (Fig. 5). The screening of activity-dependent signaling molecules in ex vivo slice cultures would help to determine if neuronal activity exerts distinct actions on OL differentiation and internode length.

Global disruption of axonal neurotransmission via expression of a tetanus neurotoxin (TeNT) reduces both myelination and the number of internodes formed per OL in larval zebrafish[39]. However, silencing of global axonal activity by TeNT expression has no effect on internode length[39]. Interestingly, another study in zebrafish detected a reduction in internode length when activity was selectively silenced in a subset of *phox2b*$^{+}$ spinal cord axons, but not when activity was silenced globally with TTX[40]. These discrepancies may arise through a competition-based interaction between adjacent axons since global suppression of activity by TTX prevented the reduction in internode length in TeNT expressing *phox2b*$^{+}$ axons. Developmental differences may also account for the discrepancy between findings from Zebrafish and the present study since the former data were obtained from larval CNS at the onset of spinal cord myelination (~ 4 days post fertilization), while the present $_{T}$OL data where obtained at least 1 week after the onset of myelination in cerebellar white matter[41]. Indeed, the newly emerging internodes analysed in Zebrafish are considerable shorter (~ 10 µm) than the shortest putative $_{T}$OL internodes detected in the present work (~ 29 µm). Whether the activity-dependent competition-based interactions detected in the larval zebrafish CNS operate at later stages of OL development in fish, or in the mammalian CNS, remains an open question.

In conclusion, the morphological analysis of SFV-labelled slice cultures enabled us to detect structural changes in individual cerebellar $_{T}$OL including the early stages of OL degeneration during complement-mediated myelin injury, and more subtle morphological changes resulting from the blockade of neuronal activity that reflect changes observed in the degree of axonal myelination. Live-imaging studies based on this approach could be used to refine our understanding of OL injury and explore the neurochemical mechanisms supporting myelin plasticity.

Methods

Animals. The data reported in this study were entirely derived from ex vivo studies, hence no live animals were used in this work. Organotypic cerebellar slice cultures were obtained from 50% C57BL/6J 50% CBA/CaCrl mice bred at the University of Warwick (Establishment License Number 30/2308) , or from either C57BL/6J mice or CNPase-GFP mice[23] bred at the University of Birmingham. CNPase-GFP mice, originally produced in the laboratory of Dr Vitorrio Gallo (Children's National Medical Center, Washington, D.C.), were rederived from frozen embryos cryo-stored by Professor Attila Sik (University of Birmingham). Mice were killed by a skilled and competent researcher using humane methods proscribed in Schedule 1 of the UK Government Animals (Scientific Procedures) Act 1986.

Organotypic slice cultures. Slice cultures were prepared and cultured as described in[5]. In brief, parasagittal vibratome slices (350 µm) cut from the cerebellum of P8-11 mice were cultured on small pieces of confetti membrane (Merk Millipore, MA, USA) placed on top of culture inserts (Merk Millipore). Mice of age P6 were used for the experiments reported in Fig. 5. Slices were cultured in 1 mL of culture media containing 50% MEM with Glutamax (Life Technologies Ltd, Paisley, UK), 23% EBSS (Life Technologies Ltd, Paisley, UK), 25% horse serum (Sigma-Aldrich Company Ltd, Dorset, UK), 6.5 mg/mL glucose, and 1250 units penicillin/streptomycin. Slices were maintained in a humidified incubator (37 °C, 5% CO_2) for 7–10 days with media changes every 2–3 days. In some experiments, slices were incubated in TTX (1 µM, Ascent Scientific, Cambridge, UK) to block neuronal activity. TTX incubations began at 0 DIV and were continued for 7 days with the medium/TTX replaced every 3 days.

3-D reconstruction of SFV-labelled OL. 3-D reconstructions were prepared from SFV-labelled OL (see Supplementary Materials and Methods online) using NeuronStudio software (Computational Neurobiology and Imaging Center, Icahn School of Medicine at Mount Sanai[42]) and FIJI Simple Neurite Tracer[43]. Cells were traced manually by viewing images in three-dimensions using the Stack Viewer mode and the resulting reconstructions exported as swc files. For an illustration of the tracing method and the resulting 3-D reconstruction, see supplementary movie 1. For methods used to analyse the morphology of OL and internodes see Supplementary Materials and Methods (online).

Statistical analysis. Normal distributions in each data set were evaluated by the Shapiro–Wilk test. Two-group comparisons of normally distributed data were performed with *t* tests, while non-normal data were analysed using the Mann–Whitney *U* test. Statistical calculations were performed using Prism 7.0 (Graphpad Software, El Camino Real, CA, USA). Reliable differences between groups were accepted at a two-tailed $P_{\alpha} < 0.05$. Normal data are presented as mean ± SEM, while non-normal data are presented as median ± interquartile range (Q1–Q3).

Additional methods can be viewed in the Supplementary Materials and Methods section online.

Ethical approval. All animal use in this work was performed in accordance with Schedule 1 of the UK Government Animals (Scientific Procedures) Act 1986. CNPase-GFP mice were bred under a Home Office project license designated for the breeding and supply of genetically modified mice. The use of transgenic mice was approved by the University of Birmingham's Animal Welfare and Ethical Review Board.

Data availability

Data sets for the 3-D reconstructions presented in this work are available at http://neuromorpho.org/.

Received: 30 September 2019; Accepted: 7 April 2021
Published online: 05 May 2021

References

1. Bartzokis, G. *et al.* Lifespan trajectory of myelin integrity and maximum motor speed. *Neurobiol. Aging* **31**, 1554–1562. https://doi.org/10.1016/j.neurobiolaging.2008.08.015 (2010).
2. Chevalier, N. *et al.* Myelination is associated with processing speed in early childhood: Preliminary insights. *PLoS ONE* **10**, e0139897. https://doi.org/10.1371/journal.pone.0139897 (2015).
3. Waxman, S. G. & Swadlow, H. A. The conduction properties of axons in central white matter. *Prog. Neurobiol.* **8**, 297–324 (1977).
4. Demerens, C. *et al.* Induction of myelination in the central nervous system by electrical activity. *Proc. Natl. Acad. Sci. U.S.A.* **93**, 9887–9892 (1996).
5. Fannon, J., Tarmier, W. & Fulton, D. Neuronal activity and AMPA-type glutamate receptor activation regulates the morphological development of oligodendrocyte precursor cells. *Glia* **63**, 1021–1035. https://doi.org/10.1002/glia.22799 (2015).
6. Lundgaard, I. *et al.* Neuregulin and BDNF induce a switch to NMDA receptor-dependent myelination by oligodendrocytes. *PLoS Biol.* **11**, e1001743 (2013).
7. Gibson, E. M. *et al.* Neuronal activity promotes oligodendrogenesis and adaptive myelination in the mammalian brain. *Science (New York, N.Y.)* **344**, 1252304 (2014).
8. Makinodan, M., Rosen, K. M., Ito, S. & Corfas, G. A critical period for social experience-dependent oligodendrocyte maturation and myelination. *Science (New York, N.Y.)* **337**, 1357–1360 (2012).
9. Fields, R. D. White matter in learning, cognition and psychiatric disorders. *Trends Neurosci.* **31**, 361–370. https://doi.org/10.1016/j.tins.2008.04.001 (2008).
10. Almeida, R. G. & Lyons, D. A. On myelinated axon plasticity and neuronal circuit formation and function. *J. Neurosci.* **37**, 10023–10034. https://doi.org/10.1523/JNEUROSCI.3185-16.2017 (2017).
11. Fields, R. D. A new mechanism of nervous system plasticity: Activity-dependent myelination. *Nat. Rev. Neurosci.* **16**, 756–767. https://doi.org/10.1038/nrn4023 (2015).
12. Mount, C. W. & Monje, M. Wrapped to adapt: Experience-dependent myelination. *Neuron* **95**, 743–756. https://doi.org/10.1016/j.neuron.2017.07.009 (2017).
13. Waxman, S. G. Determinants of conduction velocity in myelinated nerve fibers. *Muscle Nerve* **3**, 141–150. https://doi.org/10.1002/mus.880030207 (1980).
14. Wu, L. M., Williams, A., Delaney, A., Sherman, D. L. & Brophy, P. J. Increasing internodal distance in myelinated nerves accelerates nerve conduction to a flat maximum. *Curr. Biol.* **22**, 1957–1961. https://doi.org/10.1016/j.cub.2012.08.025 (2012).
15. Hughes, E. G., Orthmann-Murphy, J. L., Langseth, A. J. & Bergles, D. E. Myelin remodeling through experience-dependent oligodendrogenesis in the adult somatosensory cortex. *Nat. Neurosci.* **21**, 696–706. https://doi.org/10.1038/s41593-018-0121-5 (2018).
16. Hamilton, N. B. *et al.* Endogenous GABA controls oligodendrocyte lineage cell number, myelination, and CNS internode length. *Glia* **65**, 309–321. https://doi.org/10.1002/glia.23093 (2017).
17. Rassul, S. M., Neely, R. K. & Fulton, D. Live-imaging in the CNS: New insights on oligodendrocytes, myelination, and their responses to inflammation. *Neuropharmacology* **110**, 594–604. https://doi.org/10.1016/j.neuropharm.2015.09.011 (2016).
18. Ehrengruber, M. U. *et al.* Semliki Forest virus A7(74) transduces hippocampal neurons and glial cells in a temperature-dependent dual manner. *J. Neurovirol.* **9**, 16–28 (2003).
19. Haber, M., Vautrin, S., Fry, E. J. & Murai, K. K. Subtype-specific oligodendrocyte dynamics in organotypic culture. *Glia* **57**, 1000–1013 (2009).
20. Hardy, R. J. & Friedrich, V. L. Jr. Progressive remodeling of the oligodendrocyte process arbor during myelinogenesis. *Dev. Neurosci.* **18**, 243–254. https://doi.org/10.1159/000111414 (1996).
21. Ehrengruber, M. U., Schlesinger, S. & Lundstrom, K. Alphaviruses: Semliki forest virus and Sindbis virus vectors for gene transfer into neurons. *Curr. Protoc. Neurosci.* **4**, 422 (2011).
22. Bernardinelli, Y. *et al.* Astrocytes display complex and localized calcium responses to single-neuron stimulation in the hippocampus. *J. Neurosci.* **31**, 8905–8919. https://doi.org/10.1523/JNEUROSCI.6341-10.2011 (2011).
23. Belachew, S., Yuan, X. & Gallo, V. Unraveling oligodendrocyte origin and function by cell-specific transgenesis. *Dev. Neurosci.* **23**, 287–298. https://doi.org/10.1159/000048712 (2001).
24. Haber, M., Zhou, L. & Murai, K. K. Cooperative astrocyte and dendritic spine dynamics at hippocampal excitatory synapses. *J. Neurosci.* **26**, 8881–8891 (2006).

25. Wigley, R., Hamilton, N., Nishiyama, A., Kirchhoff, F. & Butt, A. M. Morphological and physiological interactions of NG2-glia with astrocytes and neurons. *J. Anat.* **210**, 661–670 (2007).
26. Ioannidou, K., Anderson, K. I., Strachan, D., Edgar, J. M. & Barnett, S. C. Time-lapse imaging of the dynamics of CNS glial-axonal interactions in vitro and ex vivo. *PLoS ONE* **7**, e30775. https://doi.org/10.1371/journal.pone.0030775 (2012).
27. Butt, A. M. & Ransom, B. R. Morphology of astrocytes and oligodendrocytes during development in the intact rat optic nerve. *J. Comp. Neurol.* **338**, 141–158. https://doi.org/10.1002/cne.903380110 (1993).
28. Harrer, M. D. *et al.* Live imaging of remyelination after antibody-mediated demyelination in an ex-vivo model for immune mediated CNS damage. *Exp. Neurol.* **216**, 431–438 (2009).
29. Dumas, L. *et al.* Multicolor analysis of oligodendrocyte morphology, interactions, and development with Brainbow. *Glia* **63**, 699–717. https://doi.org/10.1002/glia.22779 (2015).
30. Kirby, B. B. *et al.* In vivo time-lapse imaging shows dynamic oligodendrocyte progenitor behavior during zebrafish development. *Nat. Neurosci.* **9**, 1506–1511. https://doi.org/10.1038/nn1803 (2006).
31. Ainger, K. *et al.* Transport and localization of exogenous myelin basic protein mRNA microinjected into oligodendrocytes. *J. Cell Biol.* **123**, 431–441 (1993).
32. Butt, A. M., Colquhoun, K., Tutton, M. & Berry, M. Three-dimensional morphology of astrocytes and oligodendrocytes in the intact mouse optic nerve. *J. Neurocytol.* **23**, 469–485 (1994).
33. Young, K. M. *et al.* Oligodendrocyte dynamics in the healthy adult CNS: Evidence for myelin remodeling. *Neuron* **77**, 873–885. https://doi.org/10.1016/j.neuron.2013.01.006 (2013).
34. Chong, S. Y. *et al.* Neurite outgrowth inhibitor Nogo-A establishes spatial segregation and extent of oligodendrocyte myelination. *Proc. Natl. Acad. Sci. U.S.A.* **109**, 1299–1304. https://doi.org/10.1073/pnas.1113540109 (2012).
35. Liu, Y. *et al.* Myelin-specific multiple sclerosis antibodies cause complement-dependent oligodendrocyte loss and demyelination. *Acta Neuropathol. Commun.* **5**, 25. https://doi.org/10.1186/s40478-017-0428-6 (2017).
36. Genain, C. P., Cannella, B., Hauser, S. L. & Raine, C. S. Identification of autoantibodies associated with myelin damage in multiple sclerosis. *Nat. Med.* **5**, 170–175. https://doi.org/10.1038/5532 (1999).
37. Zhou, D. *et al.* Identification of a pathogenic antibody response to native myelin oligodendrocyte glycoprotein in multiple sclerosis. *Proc. Natl. Acad. Sci. U.S.A.* **103**, 19057–19062. https://doi.org/10.1073/pnas.0607242103 (2006).
38. Etxeberria, A. *et al.* Dynamic modulation of myelination in response to visual stimuli alters optic nerve conduction velocity. *J. Neurosci.* **36**, 6937–6948. https://doi.org/10.1523/JNEUROSCI.0908-16.2016 (2016).
39. Mensch, S. *et al.* Synaptic vesicle release regulates myelin sheath number of individual oligodendrocytes in vivo. *Nat. Neurosci.* **18**, 628–630. https://doi.org/10.1038/nn.3991 (2015).
40. Hines, J. H., Ravanelli, A. M., Schwindt, R., Scott, E. K. & Appel, B. Neuronal activity biases axon selection for myelination in vivo. *Nat. Neurosci.* **18**, 683–689. https://doi.org/10.1038/nn.3992 (2015).
41. Bouslama-Oueghlani, L., Wehrle, R., Sotelo, C. & Dusart, I. The developmental loss of the ability of Purkinje cells to regenerate their axons occurs in the absence of myelin: An in vitro model to prevent myelination. *J. Neurosci.* **23**, 8318–8329 (2003).
42. Wearne, S. L. *et al.* New techniques for imaging, digitization and analysis of three-dimensional neural morphology on multiple scales. *Neuroscience* **136**, 661–680 (2005).
43. Longair, M. H., Baker, D. A. & Armstrong, J. D. Simple Neurite Tracer: Open source software for reconstruction, visualization and analysis of neuronal processes. *Bioinformatics* **27**, 2453–2454. https://doi.org/10.1093/bioinformatics/btr390 (2011).

Acknowledgements

This work was supported by a fellowship to D.F. from the Birmingham Science City Research Alliance funded by the Higher Education Funding Council for England (HEFCE), a grant from the People Programme (Marie Curie Actions) of the European Union's Seventh Framework Programme (CIG 294051), and the University of Birmingham's Wellcome Trust Institutional Strategic Support Fund (2014 round). S.M.R. was supported by funding from the Engineering and Physical Sciences Research Council through a studentship from the Physical Sciences of Imaging in the Biomedical Sciences Doctoral Training Centre (EP/F50053X/1). We thank Dr Zubair Ahmed (Institute of Inflammation and Ageing, University of Birmingham) for his useful comments on the manuscript, and Professor Pranab Das (University of Birmingham) for discussions and advice on complement-mediated injury.

Author contributions

Concept and design of the study: D.F.; design and generation of SFVA7(74)mCherry-MBP vector: S.M.R. and D.F.; data acquisition D.F., data analysis: E.T. and D.F.; drafting of manuscript and figures: M.B. and D.F. All authors read and approved the submitted version of the manuscript.

Competing interests

The authors declare no competing interests.

Additional information

Supplementary Information The online version contains supplementary material available at https://doi.org/10.1038/s41598-021-88887-0.

Correspondence and requests for materials should be addressed to D.F.

Reprints and permissions information is available at www.nature.com/reprints.

Publisher's note Springer Nature remains neutral with regard to jurisdictional claims in published maps and institutional affiliations.